

Single-band to two-band superconductivity transition in two-dimensional oxide interfaces.

G. Singh^{1,2}, A. Jouan^{1,2}, G. Herranz³, M. Scigaj³, F. Sánchez³, L. Benfatto^{4,5}, S. Caprara^{5,4},
M. Grilli^{5,4}, G. Saiz^{1,2}, F. Couedo^{1,2}, C. Feuillet-Palma^{1,2}, J. Lesueur^{1,2}, N. Bergeal^{1,2*}

¹*Laboratoire de Physique et d'Etude des Matériaux,
ESPCI Paris, PSL Research University, CNRS,
10 Rue Vauquelin - 75005 Paris, France.*

²*Université Pierre and Marie Curie,
Sorbonne-Universités, 75005 Paris, France.*

³*Institut de Ciència de Materials de Barcelona (ICMAB-CSIC),
Campus de la UAB, 08193 Bellaterra, Catalonia,
Spain.*

⁴*Institute for Complex Systems (ISC-CNR),
UOS Sapienza, Piazzale A. Moro 5, 00185 Roma, Italy*

⁵*Dipartimento di Fisica Università di Roma "La Sapienza",
Piazzale A. Moro 5, I-00185 Roma, Italy.*

In multiorbital materials, superconductivity can exhibit new exotic forms that include several coupled condensates. In this context, quantum confinement in two-dimensional superconducting oxide interfaces offers new degrees of freedom to engineer the band structure and selectively control $3d$ -orbitals occupancy by electrostatic doping. However, the presence of multiple superconducting condensates in these systems has not yet been demonstrated. Here, we use resonant microwave transport to extract the superfluid stiffness of the (110)-oriented $\text{LaAlO}_3/\text{SrTiO}_3$ interface in the entire phase diagram. We evidence a transition from single-band to two-band superconductivity driven by electrostatic doping, which we relate to the filling of the different $3d$ -orbitals based on numerical simulations of the quantum well. Interestingly, the superconducting transition temperature decreases while the second band is populated, which challenges the Bardeen-Cooper-Schrieffer theory. To explain this behaviour, we propose that the superconducting order parameters associated with the two bands have opposite signs with respect to each other.

In cubic perovskites, transition metal ions are surrounded by six oxygen ions in an octahedron configuration. Because of the negative charge of O^{2-} ions, the transition metal $3d$ electrons are subject to an anisotropic crystal field, which splits the five $3d$ orbitals into three degenerated

t_{2g} orbitals (d_{xy} , d_{xz} and d_{yz}) and two degenerated e_g orbitals ($d_{x^2-y^2}$ and d_{z^2}) at higher energy [1]. This situation is encountered in bulk SrTiO_3 crystals whose conduction band is formed by the coupling between t_{2g} orbitals at neighbouring Ti lattice sites through the $2p$ orbitals of the oxygen atoms. Meanwhile, the physical properties of two-dimensional SrTiO_3 -based interfaces such as $\text{LaAlO}_3/\text{SrTiO}_3$ [2, 3] or $\text{LaTiO}_3/\text{SrTiO}_3$ [4] interfaces are also deeply affected by the further splitting of the t_{2g} bands under quantum confinement. Many theoretical works have shown that a complex band structure involving bands with different orbital symmetries is generated at the interface [5–9]. These predictions are supported by experiments such as x-ray absorption spectroscopy [10], optical conductivity [11], Hall effect [12–14] and quantum oscillations [15–17], which evidence multiband transport at high carrier densities. The presence of several disconnected Fermi surface sheets makes these materials more prone to exhibit unconventional properties.

One of the main challenges in understanding superconductivity in multiband systems is to identify the connection between superconductivity and the different band occupancies. In the conventional weak-coupling BCS theory, the superconducting critical temperature is expressed as $T_c \simeq \hbar\omega_D e^{-\frac{1}{\lambda}}$, where $\hbar\omega_D$ is an energy cutoff (Debye energy in the standard phonon-mediated pairing mechanism) and $\lambda = N(0)V_0$ is the coupling constant [18]. Because of the exponential factor, the density of states at the Fermi level, $N(0)$ and the pairing potential, V_0 , are the most relevant parameters in the determination of T_c . Although the origin of superconductivity in SrTiO_3 is still debated, it is widely believed that its gigantic low-temperature dielectric constant $\epsilon_R \simeq 25000$ [19] should play a pivotal role in the pairing mechanism and consequently in the determination of V_0 . On the other hand, in a two-dimensional system, the density of states is directly proportional to the effective mass m^* of the carriers, $N(0) = \frac{m^*}{\pi\hbar^2}$. Whereas these two parameters are fixed in a bulk material, oxide interfaces offer several possibilities to vary $N(0)$ and V_0 , for instance by selecting t_{2g} orbitals through crystal orientation [20] or by electrostatic control of the band fillings. Here, we use resonant microwave transport to investigate the superfluid stiffness of the (110)-oriented interface. In contrast with the reported single band superconductivity in the conventional (001)-oriented interfaces [21–23], we demonstrate the presence of two superconducting coupled condensates at high carrier doping, which we relate to the degenerated d_{xz}/d_{yz} bands on the one hand and the d_{xy} band on the other hand. Because of the unusual decrease of T_c concomitant with the emergence of the second band, we propose that the two condensate are coupled by a repulsive interaction leading to opposite-sign gaps $s\pm$ -wave superconductivity.

While most studies have focused on (001)-oriented $\text{LaAlO}_3/\text{SrTiO}_3$ heterostructures, it has been recently shown that a superconducting two-dimensional electron gas (2-DEG) can also develop

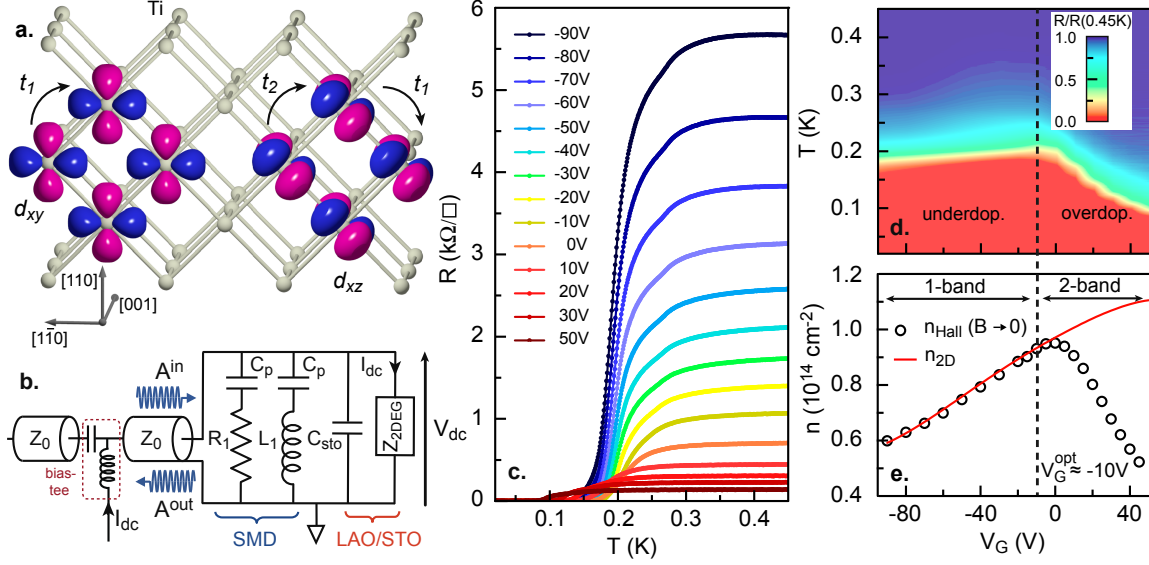


Figure 1: **Superconductivity and multiband transport in (110)-oriented LaAlO₃/SrTiO₃ interfaces.** a) Scheme of the t_{2g} orbitals in the (110)-oriented SrTiO₃. d_{yz} orbitals (not shown) are obtained by a 90° rotation of the d_{xz} ones along the (001) direction. t_1 and t_2 represent the hopping terms along the different directions. In this experiment current was injected along the (1-10) direction. b) Resonant sample circuit comprising the LaAlO₃/SrTiO₃ heterostructure (Z_{2DEG} and C_{sto}) and the SMD components, $R_1=100\ \Omega$ and $L_1=9\ nH$. $C_p=2\ \mu F$ are protective capacitances that avoid dc current to flow through L_1 and R_1 without influencing the resonance frequency of the circuit ω_0 [22]. A bias-tee is used to separate the dc signal from the RF one. c) Sheet resistance as a function of temperature measured in dc for different gate voltages in the range [-90V,+50]. (d) Sheet resistance normalized by its value at $T=0.45K$ in color scale as a function of gate voltage and temperature. (e) Hall carrier density n_{Hall} measured at $T=3K$ in the limit $B \rightarrow 0$ as a function of V_G . The gate dependence of the 2D carrier density n_{2D} has been obtained by integrating the gate capacitance and by matching it to n_{Hall} in the one-band regime ($V_G < -10V$) (see Methods).

in other crystal orientations, such as the (110) direction [20] and the (111) direction [24–26]. In this study, we used 10 uc-thick LaAlO₃ epitaxial layers grown on 3×3 mm² (110)-oriented SrTiO₃ substrate by Pulsed Laser Deposition (see Methods section) [20]. The orientation of the t_{2g} orbitals in this heterostructure is shown in Fig. 1a. Because of the symmetry of the orbitals, the ability of electrons to hop between two neighbouring Ti lattice sites strongly depends on the spatial directions, which causes anisotropic band properties. After the growth, a weakly conducting metallic back-gate of resistance $\sim 100\ k\Omega$ was deposited on the backside of the 200 μm -thick substrate. The LaAlO₃/SrTiO₃ heterostructure was inserted in a microwave circuit board between the central strip of a coplanar waveguide transmission line and its ground to perform microwave measurements as described in reference [22]. The Surface Mounted microwave Devices (SMD), which include resistor R_1 and inductor L_1 , were added to form a parallel RLC resonant circuit, where the capacitance C_{STO} is the intrinsic capacitance of the SrTiO₃ substrate (Fig. 1b). After cooling the sample to 450 mK, the first positive polarization was applied to a maximum gate voltage

$V_G=+50$ V to ensure that no hysteresis would occur upon further gating [27]. Figure 1c displays the temperature-dependent sheet resistance R of the 2-DEG, which was measured in dc for different gate voltages in the range $[-90\text{V}, +50\text{V}]$. A clear superconducting transition to a zero resistive state is observed for all gate values. The resulting phase diagram, obtained by plotting the normalized resistance in colour scale as a function of temperature and gate voltage is shown in Fig. 1d. In contrast with the conventional (001)-orientation [3, 12, 28], superconductivity can not be suppressed by carrier depletion. In the underdoped (UD) regime, the transition temperature weakly increases with V_G to a maximum value of $\simeq 200$ mK at the optimal doping $V_G^{\text{opt}} \simeq -10$ V, before decreasing in the overdoped (OD) regime ($V_G > V_G^{\text{opt}}$).

To understand this unexpected gate dependence, we analyse the Hall effect in the normal state of the 2-DEG. Whereas the Hall resistance R_H is linear with the magnetic field B at low-doping, corresponding to one-band transport (labelled band 1), this is not the case at high doping (Supplementary Figure 1). This suggests that a one-band to two-band transition occurs in the Hall effect for a certain gate voltage. The variation of the 2-DEG carrier density n_{2D} over the entire phase diagram, can be retrieved by plotting the charging curve of the capacitor (Fig. 1e) (see Methods). The new band (band 2) filling threshold corresponds to the gate value where $n_{\text{Hall}} = \frac{B}{eR_H}$ measured in the limit $B \rightarrow 0$, deviates from n_{2D} [12, 29]. Interestingly, this change in Hall behaviour occurs at the optimal doping point ($V_G^{\text{opt}} \simeq -10\text{V}$), which establishes a correlation between the OD superconducting regime and the two-band transport regime observed in the normal state. However, the significant decrease of transition temperature in this regime also indicates that the filling of band 2 is detrimental for superconductivity.

We further investigated the superconducting properties of the (110)-oriented $\text{LaAlO}_3/\text{SrTiO}_3$ interfaces by measuring their superfluid stiffness J_s , which characterizes the phase rigidity of the condensate. This fundamental energy scale is directly related to the imaginary part of the complex conductivity of the superconductor $\sigma_2(\omega)$ at finite frequency [30, 31]

$$J_s = \frac{\hbar^2 \sigma_2(\omega) \omega}{4e^2} = \frac{\hbar^2}{4e^2 L_k} \quad (1)$$

where L_k is the kinetic inductance of the superconductor due of the inertia of the Cooper pairs. In the normal state ($T = 0.45$ K $> T_c$), $\sigma_2(\omega)=0$ and the sample circuit described in Fig. 1b resonates at the frequency $\omega_0 = \frac{1}{\sqrt{L_1 C_{\text{sto}}}}$, which can be determined by measuring the reflection coefficient of the sample circuit $\Gamma(\omega) = \frac{A_{\text{in}}}{A_{\text{out}}}$ (Fig. 1b). The resonance manifests itself as a dip in the magnitude of $\Gamma(\omega)$ accompanied by a 2π phase shift (Supplementary Figure 2) [22]. Figure 2 shows the temperature dependence of the reflection coefficient for a selection of gate voltages. In

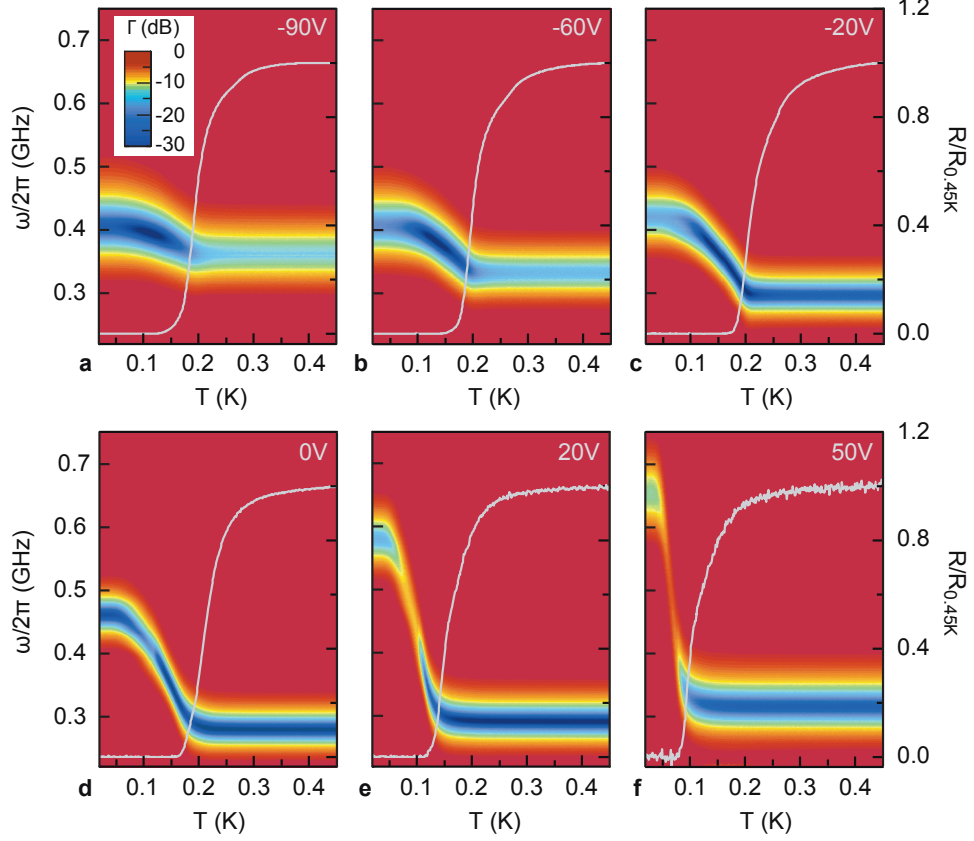


Figure 2: **Resonant microwave transport in the superconducting state.** (a-f) Magnitude of $\Gamma(\omega)$ in dB as a function of temperature for different values of the gate voltage after calibration [22]. The normalized sheet resistance as a function of temperature is shown on the right axis.

the superconducting state, the 2-DEG conductance acquires an imaginary part $\sigma_2(\omega) = \frac{1}{L_k\omega}$ that generates a shift of ω_0 towards high frequencies since the total inductance of the circuit becomes $L_{\text{tot}}(T) = \frac{L_1 L_k(T)}{L_1 + L_k(T)}$. The superfluid stiffness $J_s(T)$ is thus extracted from the resonance shift for all gate values using Eq. (1).

For a single-band superconductor, the temperature dependence of the normalized stiffness $j_s(T) = \frac{J_s(T)}{J_s(0)}$ can be derived from the BCS superconducting gap energy $\Delta(T)$ [32]

$$j_s = \delta^2 \sum_{n=0}^{\infty} [\delta^2 + (n + 1/2)^2]^{-3/2} \quad (2)$$

where $\delta = \frac{\Delta(T)}{2\pi k_B T}$ is the dimensionless gap energy and n is an integer that defines the Matsubara frequencies $\hbar\omega = \pi T(2n + 1)$. In Figure 3 we compare the temperature dependence of j_s in the underdoped (UD) and overdoped (OD) regions of the phase diagram. Two distinct behaviors can be identified. In the UD regime, all the curves overlap each other and follow a single-gap BCS

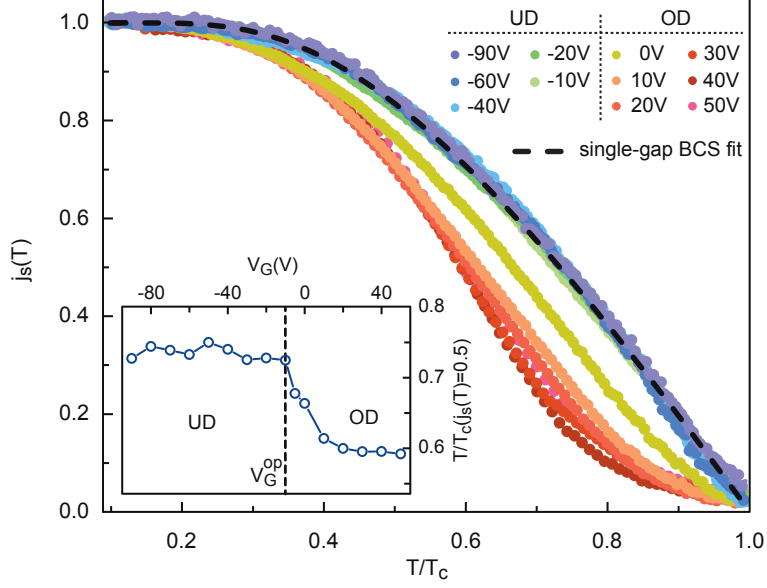


Figure 3: **Superfluid stiffness in the underdoped and overdoped regimes.** Normalized superfluid stiffness $j_s(T)$ as a function of the reduced temperature $\frac{T}{T_c}$ for different gate voltages spanning the underdoped (UD) and overdoped (OD) regimes. The value of T_c used in the reduced temperature is the one extracted from the fit of Fig 4. In the UD regime, all the curves are superimposed and follow a single-gap BCS behavior (dashed line). In the OD regime, the temperature dependence of the $j_s(T)$ curve is strongly modified. The absolute value of J_s at $T \simeq 0$ as a function of V_G is shown in Supplementary Figure 3. Inset) Reduced temperature corresponding to a reduction of 50% of the normalized stiffness. Whereas the values are constant in the UD regime, an abrupt decrease takes place in the OD regime.

behavior (Eq. 2) in consistency with the single band Hall effect reported in Fig. 1e. On the other hand, in the OD regime, j_s shows a strong deviation with respect to the single-gap BCS behavior. In particular, a change in curvature and a prominent tail appear for $j_s < 0.5$. The inset of Fig. 3 emphasizes this difference in trend by showing the reduced temperature $\frac{T}{T_c}$ corresponding to a reduction of 50% of j_s as a function of gate voltage. Whereas this value is constant in the UD regime, it drops abruptly at V_G^{opt} and further decreases in the OD regime. This result clearly suggests that a transition between single-band superconductivity and two-band superconductivity occurs at V_G^{opt} due to the filling of band 2 as anticipated from Hall effect (Fig. 1e). To calculate the superfluid stiffness in two-band superconductors, Kogan *et al.* developed a self-consistent BCS approach based on the quasi-classical Eilenberger weak coupling formalism [32, 33]. First, the two superconducting gaps $\Delta_1(T)$ and $\Delta_2(T)$ are self-consistently calculated by introducing the intraband (λ_{11} , λ_{22}) and interband (λ_{12} , λ_{21}) coupling constants (Supplementary Note 1). Then, the temperature dependence of the normalized stiffness for each band j_{s1} and j_{s2} is obtained by introducing the corresponding gaps Δ_1 and Δ_2 in Eq (2). The total normalized stiffness is the sum of the contributions of each

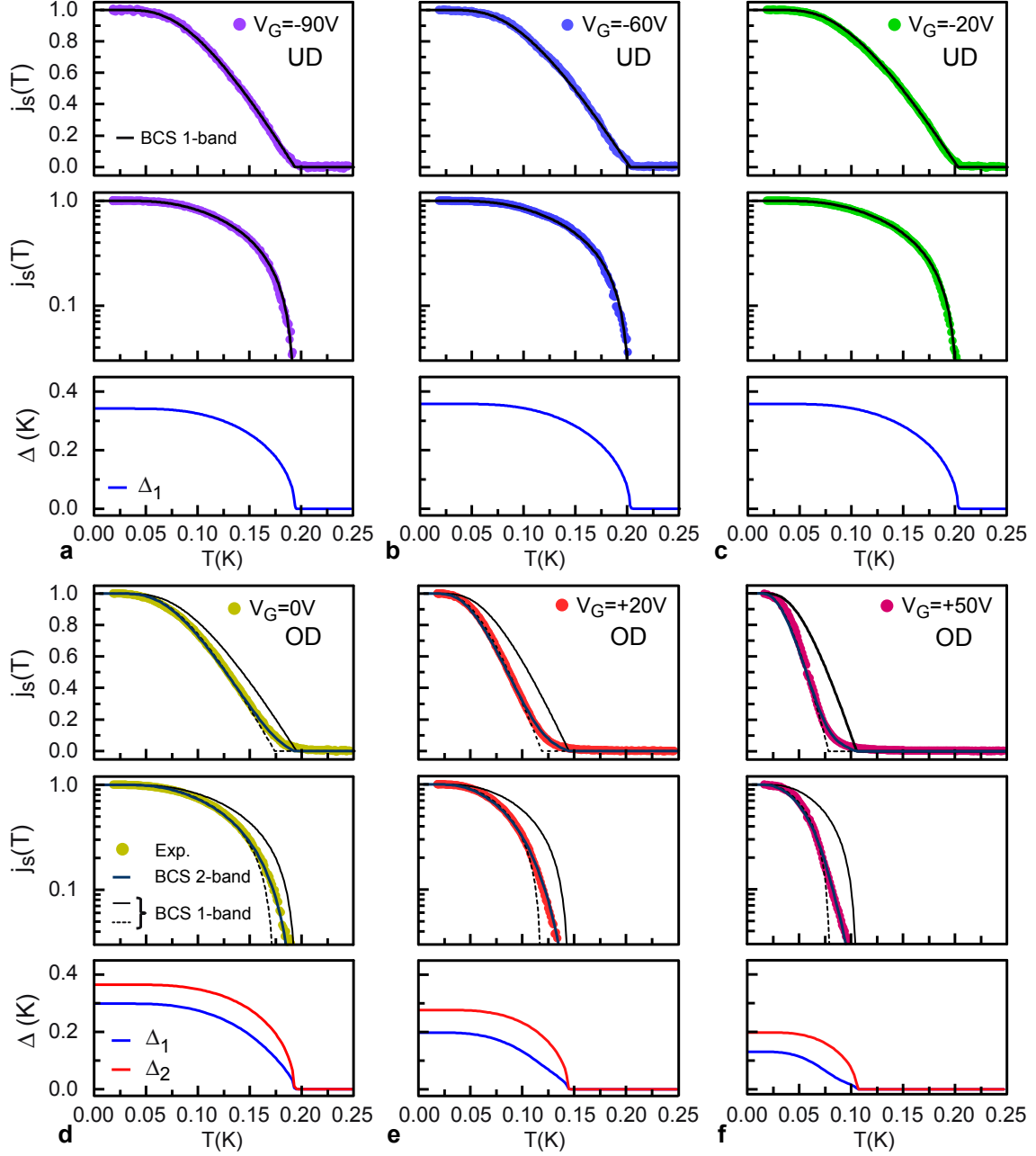


Figure 4: **Single-band to two-band superconductivity transition in the superfluid stiffness.** Temperature dependence of j_s (symbols) in linear scale (upper panels) and logarithmic scale (middle panels) for three gate voltages in the UD regime ((a) $V_G = -90V$, (b) $V_G = -60V$ and (c) $V_G = -20V$) and three gate voltages in the OD regime ((d) $V_G = 0V$, (e) $V_G = 20V$ and (f) $V_G = 50V$). In the UD regime, $j_s(T)$ is fitted using the single-band model (black line) assuming in Eq. (2) the gap energy $\Delta_1(T)$ shown in the lower panel for each gate voltage. In the OD regime, $j_s(T)$ is fitted using the two-band model (blue line) corresponding to Eq. (3), assuming in Eq. (2) the gap energies $\Delta_1(T)$ and $\Delta_2(T)$ shown in the lower panel for each gate voltage. The values of the γ coefficient and coupling constants are given in Supplementary Figure 5 and 6. Two attempts to fit $j_s(T)$ in the overdoped regime with different T_c using a single-band model are also shown (black and dashed lines). The fit at optimal doping $V_G^{\text{opt}} = -10V$ is shown in supplementary figure 4.

band [32]

$$j_s = \gamma j_{s1} + (1 - \gamma) j_{s2} \quad (3)$$

where the γ coefficient accounts for the weight of each band in the superfluid condensate. A systematic fitting procedure based on this approach was applied to j_s . As shown in Fig. 4 for different gate voltages spanning both the UD regime (panels a,b and c) and the OD regime (panels d,e and f), a very good agreement is obtained between the experimental data and the BCS model. In particular, the transition between single-band and two-band superconductivity is clearly visible both in linear scale (up sub-panels) and logarithmic scale (middle sub-panels). In the OD regime, the change in curvature and the tail in $j_s(T)$ curves are well described by the model considering a weak interband coupling ($|\lambda_{12(21)}| \ll \lambda_{11(22)}$). In this case, the largest gap (Δ_2) is only weakly affected by this coupling and behaves essentially as a single BCS gap closing at T_c (low sub-panels). On the other hand, the smallest gap (Δ_1) follows a BCS trend at low temperature but instead of closing at a correspondingly lower transition temperature, it extends to T_c . This generates a change in curvature and a tail which is further reproduced in $j_s(T)$. The fits implies that the band with the smallest gap and the tail contributes to the total superfluid stiffness with the strongest weight. According to the band hierarchy in the quantum well, this must correspond to band 1, which is mainly filled. Fig. 5c summarizes the values of the superconducting gap energies in the phase diagram extracted from the fitting procedure. In the underdoped regime, $\Delta_1(0)$ very weakly increases with V_G , which is consistent with BCS theory since for a 2D superconductor, T_c is in principle carrier density independent (in absence of other mechanisms affecting λ_{11}). In the overdoped regime, band 2 is also filled, and a second superconducting gap Δ_2 opens at the Fermi surface, which is larger than Δ_1 . The correspondence of these bands to specific orbital symmetries is discussed below.

Arguing that superconductivity in SrTiO₃-based interfaces has likely the same origin than that of bulk SrTiO₃, early reports of a distinctive double-gap structure in the tunneling density of states in Nb-doped bulk SrTiO₃ above a certain density ($\simeq 5 \times 10^{19} \text{ cm}^{-3}$) [34] motivated the theoretical suggestion that multiband superconductivity can also take place also in LaAlO₃/SrTiO₃ heterostructures [35, 36]. While the onset of multiple-band occupancy in bulk SrTiO₃ has been recently confirmed by the analysis of quantum oscillations in the normal state [37], very recent tunneling [38] and a.c. conductivity experiments do not show any evidence for multi-gap superconductivity [39]. For heterostructures, only the conventional (001)-orientation has been theoretically considered, and in this type of interfaces, experiments [21–23] are rather consistent with the presence of a single superconducting gap. To establish a relation between the two gaps evidenced in our

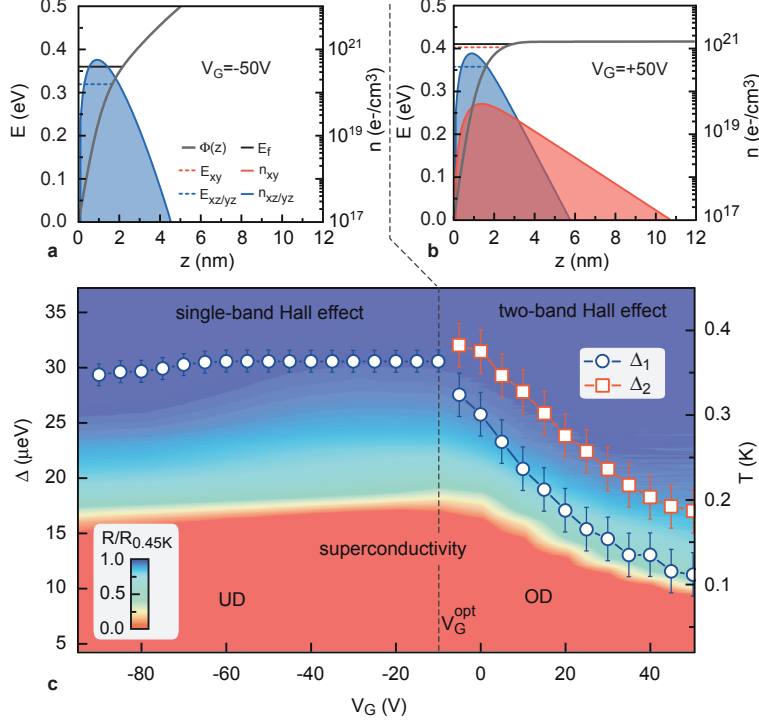


Figure 5: **Superconducting phase diagram.** a,b) Numerical simulations of the band structure in the (110)-oriented interfaces which shows the energies of the different t_{2g} bands in the confinement potential $\Phi(z)$ (left axis) and the 3D carrier densities ($n_{xy}, n_{xz/yz}$) associated to each band (right axis), obtained by solving the self-consistent Poisson-Schrödinger equations for two doping regime : $V_G = -50V$ (panel a) and $V_G = +50V$ (panel b). The 2D carrier density used in the simulation corresponds to the one reported on Fig. 1e, i. e. $n \simeq 0.75 \cdot 10^{14} \text{e}/\text{cm}^2$ at $V_G = -50V$ and $n \simeq 1.1 \cdot 10^{14} \text{e}/\text{cm}^2$ at $V_G = +50V$. See Supplementary Note 2 for details on the numerical simulation. c) Gap energies $\Delta_1(0)$ and $\Delta_2(0)$ extracted from the fitting procedure (left axis) as a function of V_G , superimposed on the sheet resistance (color scale) of the 2-DEG plotted as a function of temperature (right axis) and V_G .

experiment and the different t_{2g} bands, we numerically simulated the interfacial band structure by self-consistently solving the Poisson-Schrödinger equations (Fig. 5a-b)(see Supplementary Note 2). In this crystal orientation, the band hierarchy is reversed with respect to the conventional (001)-orientation [20, 40]. The degenerated d_{xz}/d_{yz} bands are always filled whereas the d_{xy} band at higher energy is only occupied at strong electrostatic doping. The ability of these different bands to host superconductivity critically depends on their density of states $N(0)$, which is directly proportional to their in-plane effective mass. In contrast to the (001)-oriented interfaces, where the low density of states of the d_{xy} band precludes the formation of superconductivity at low doping, in the (110)-orientation, the two bands have relatively high and similar DOS ($m_{\parallel}^{xz,yz} \simeq 2.3m_0$ and $m_{\parallel}^{xy} \simeq 3.1m_0$, see Supplementary Note 2). Consequently, they are both suitable to sustain superconductivity, which explains why superconductivity cannot be (or is hardly) suppressed by carrier depletion, and why two-band superconductivity is observed at high electrostatic gating. According to the numer-

ical simulations, we relate band 1 (Δ_1, J_{s1}) to the d_{xz}/d_{yz} band and band 2 (Δ_2, J_{s2}) to the d_{xy} band.

One of the fundamental questions that arises in two-band superconductors is whether the energy gaps in the different bands have the same sign. The temperature dependence of the superfluid density suggests that there are no nodes, so the gap must be constant over each of the two Fermi surfaces. On the other hand, the two superconducting order parameters can have the same sign (s_{++} -wave pairing) for an attractive interband interaction ($\lambda_{12(21)} > 0$) or opposite sign (s_{\pm} -wave pairing) for a repulsive interband interaction ($\lambda_{12(21)} < 0$). This issue has been widely discussed in the context of iron-based superconductors, where antiferromagnetic spin fluctuations are expected to provide a repulsive interband pairing channel [41–43], leading to s_{\pm} pairing with two nodeless gaps of opposite signs on the hole and electron pockets. The presence of multiple gaps in these systems has been confirmed by several thermodynamic probes, like e.g. the temperature dependence of the superfluid density [44]. Recently, the analysis of quasiparticle-interference imaging in STM experiments also allowed to demonstrate the sign-changing nature of the order parameter, confirming the s_{\pm} nature of superconductivity in Fe(Se,Te) and FeSe [45, 46]. According to BCS theory, only the positive quantity $\lambda_{12(21)}^2$ affects the determination of T_c . Therefore, the coupling with an additional band with a significant density of states should always lead to an increase of T_c , regardless of the sign of λ_{12} [32, 35]. This would then be in contradiction with our findings, where T_c decreases soon after that the second band is populated, see Fig. 5. However, this apparent discrepancy could be reconciled by accounting for impurity scattering in a s_{\pm} superconductor. Indeed, although nodeless single-band superconductivity is essentially insensitive to scattering (provided it is not too strong), in multiband s_{\pm} superconductors scattering processes between bands with opposite-sign gaps are pair-breaking, leading to a suppression of superconductivity [35, 47]. The mechanism is similar to the one occurring in high- T_c superconducting cuprates, where the $d_{x^2-y^2}$ superconducting order parameter changes sign between different regions of the single-band Fermi surface, making impurity scattering detrimental for superconductivity. In this view the s_{\pm} symmetry of the order parameter in our (110)-oriented LaAlO₃/SrTiO₃ interfaces could explain why the onset of superconductivity in the second band makes the system more sensitive to impurity scattering, leading to the unusual suppression of T_c observed in the OD regime. It is worth noting that the analysis of the temperature dependence of the superfluid density based on Eq. (11) relies mainly on the relative band filling and on the gap values, so it is a robust finding rather insensitive to the presence of disorder. On the other hand, the suppression of the gaps and T_c in the OD regime, that we simply modeled via a decrease of the superconducting couplings λ_{ij} in the absence of disorder, could be understood as the effect of disorder within a multiband model with constant pairing interactions and s_{\pm} gap symmetry[36].

Although the origin of the repulsive interband coupling in our system remains to be identified, we anticipate that it could be related to the specific t_{2g} orbitals symmetry of the bands.

According to the typical gap energies reported in Fig. 5c, the transition from single-band to two-band superconductivity in the (110)-oriented $\text{LaAlO}_3/\text{SrTiO}_3$ interface, can be confirmed by direct tunnelling spectroscopy using planar junctions or STM spectroscopy. However, the relative sign must be investigated using of a phase-sensitive experiment such as a Josephson experiment for example [48]. Finally, we also mention that a similar situation can occur in the conventional (001)-oriented interface whose superconducting phase diagram $T_c(V_G)$ displays a characteristic dome-shape [3, 12, 49]. Although tunnelling spectroscopy mainly reveals a single gap [21], we cannot exclude that the decrease of T_c in the overdoped regime could originate from a repulsive coupling with a reversed-sign superconducting gap that opens in a high-energy d_{xy} replica band [36]. Because $N(0)$ is weak for the d_{xy} bands in this orientation, interband scattering can contribute to the reduction of T_c but the gap may not be easily visible in either tunnelling spectra nor in superfluid stiffness.

Acknowledgments

We acknowledge K. Behnia for useful discussions. This work has been supported by the Région Ile-de-France in the framework of CNano IdF, OXYMORE and Sesame programs, by CNRS through a PICS program (S2S) and ANR JCJC (Nano-SO2DEG). This work was supported by the Spanish MAT2017-85232-R, MAT2014-56063-C2-1-R, Severo Ochoa SEV-2015-0496 grant, and the Generalitat de Catalunya (2017 SGR 1377). This work has been supported by the Italian MAECI under the Italia-India collaborative project SUPERTOP-PGR04879.

-
- [1] Imada, M. Fujimori, A. and Tokura, Y. Metal-insulator transitions. *Rev. Mod. Phys.* **70**, 1039 (1998).
 - [2] Ohtomo, A. & Hwang, H. Y. A high-mobility electron gas at the $\text{LaAlO}_3/\text{SrTiO}_3$ heterointerface. *Nature* **427**, 423–426 (2004).
 - [3] Caviglia, A. D., Gariglio, S., Reyren, N., Jaccard, D., Schneider, T., Gabay, M., Thiel, S., Hammerl, G., Mannhart, J. and Triscone, J.-M. Electric field control of the $\text{LaAlO}_3/\text{SrTiO}_3$ interface ground state. *Nature* **456**, 624–627 (2008).
 - [4] Biscaras, J., Bergeal, N., Kushwaha, A., Wolf, T., Rastogi, A., Budhani, R. C. and Lesueur, J. Two-dimensional superconductivity at a Mott insulator/band insulator interface $\text{LaTiO}_3/\text{SrTiO}_3$. *Nature Commun.* **1**, 89 (2010).
 - [5] Popovic, Z. S., Satpathy, S. and Martin, R. M. Origin of the two-dimensional electron gas carrier density at the LaAlO_3 on SrTiO_3 interface. *Phys. Rev. Lett.* **101**, 256801 (2008).
 - [6] Delugas, P. *et al.* Spontaneous 2-dimensional carrier confinement at the n-type $\text{SrTiO}_3/\text{LaAlO}_3$ interface. *Phys. Rev. Lett.* **106**, 166807 (2011).
 - [7] Pentcheva, R. and Pickett, W. Charge localization or itineracy at $\text{LaAlO}_3/\text{SrTiO}_3$ interfaces: hole polarons, oxygen

- vacancies, and mobile electrons. *Phys. Rev. B* **74**, 035112 (2006).
- [8] Pavlenko, N., Kopp, T., Tsymbal, E., Sawatzky, G. and Mannhart, J. Magnetic and superconducting phases at the $\text{LaAlO}_3/\text{SrTiO}_3$ interface: the role of interfacial Ti 3d electrons. *Phys. Rev. B* **85**, 020407(R) (2012).
- [9] Scopigno, N., Bucheli, D., Caprara, S., Biscaras, J., Bergeal, N., Lesueur, J., Grilli, M. Phase Separation from Electron Confinement at Oxide Interfaces *Phys. Rev. Lett.* **116**, 026804 (2016).
- [10] Salluzzo, M. et al. Orbital Reconstruction and the Two-Dimensional Electron Gas at the $\text{LaAlO}_3/\text{SrTiO}_3$ Interface. *Phys. Rev. Lett.* **102**, 166804 (2009).
- [11] Seo, S. S. A. et al. Multiple conducting carriers generated in $\text{LaAlO}_3/\text{SrTiO}_3$ heterostructures. *Appl. Phys. Lett.* **95**, 082107 (2009).
- [12] Biscaras, J., Bergeal, N., Hurand, S., Grossetete, C., Rastogi, A., Budhani, R. C., LeBoeuf, D., Proust, C. and Lesueur, J. Two-dimensional superconductivity induced by high-mobility carrier doping in $\text{LaTiO}_3/\text{SrTiO}_3$ heterostructures. *Phys. Rev. Lett.* **108**, 247004 (2012).
- [13] Kim, J. S., Seo, S. S. A., Chisholm, M. F., Kremer, R. K., Habermeier, H.-U., Keimer, B. and Lee, H. N. Nonlinear Hall effect and multichannel conduction in $\text{LaTiO}_3/\text{SrTiO}_3$ superlattices. *Phys. Rev. B* **82**, 201407 (2010).
- [14] Ohtsuka, R., Matvejeff, M., Nishio, N., Takahashi, R. & Lippmaa, M. Transport properties of $\text{LaTiO}_3/\text{SrTiO}_3$ heterostructures. *Appl. Phys. Lett.* **96**, 192111 (2010).
- [15] Caviglia, A. et al Two-dimensional quantum oscillations of the conductance at $\text{LaAlO}_3/\text{SrTiO}_3$ interfaces. *Phys. Rev. Lett.* **105**, 236802 (2010).
- [16] Ben Shalom, M., Ron, A., Palevski, A., Dagan, Y. Shubnikov-de Haas oscillations in $\text{SrTiO}_3/\text{LaAlO}_3$ interface. *Phys. Rev. Lett.* **105**, 206401 (2010).
- [17] Yang, M., Han, K., Torresin, O., Pierre, M., Zeng, S., Huang, Z., Venkatesan, T. V., Goiran, M., Coey, J. M. D., Ariando, and Escoffier, W. High-field magneto-transport in two-dimensional electron gas $\text{LaAlO}_3/\text{SrTiO}_3$. *Appl. Phys. Lett.* **109**, 122106 (2016).
- [18] Bardeen, J., Cooper L. N. and Schrieffer, J. R. Theory of Superconductivity. *Phys. Rev.* **108**, 1175-1204 (1957).
- [19] Neville, R. C., Hoeneisen, B and Mead, C. A., Permittivity of Strontium Titanate. *J. Appl. Phys.* **43**, 2124 (1972).
- [20] Herranz, G., Singh, G., Bergeal, N., Jouan, A., Lesueur, J., Gázquez, J., Varela, M., Scigaj, M., Dix, N., Sánchez, F. and Fontcuberta, J. Engineering two-dimensional superconductivity and Rashba spin-orbit coupling in $\text{LaAlO}_3/\text{SrTiO}_3$ quantum wells by selective orbital occupancy. *Nature Comm.* **6**, 6028 (2015).
- [21] Richter, C., Boschker, H., Dietsche, W., Fillis-Tsirakis, E., Jany, R., Loder, F., Kourkoutis, L. F., Muller, D. A., Kirtley, J. R., Schneider, C. W. and Mannhart, J. Interface superconductor with gap behaviour like a high-temperature superconductor. *Nature* **502**, 528-531 (2013).
- [22] Singh, G. et al. Competition between electron pairing and phase coherence in superconducting interfaces. *Nat. Commun.* **9**, 407 (2018).
- [23] Bert, J. A., Nowack, K. C., Kalisky, B., Noad, H., Kirtley, J. R., Bell, C., Sato, H. K., Hosoda, M. Hikita, Y., Hwang, H. Y. and Moler, K. A. Gate-tuned superfluid density at the superconducting $\text{LaAlO}_3/\text{SrTiO}_3$ interface. *Phys. Rev. B* **86**, 060503(R) (2012).
- [24] Monteiro, A. M. R. V. L., Groenendijk, D. J., Groen, I., de Bruijckere, J., Gaudenzi, R., van der Zant, H. S. J. and Caviglia A. D. Two-dimensional superconductivity at the (111) $\text{LaAlO}_3/\text{SrTiO}_3$ interface *Phys. Rev. B* , **96** 020504(R) (2017).
- [25] Rout, P. K., Maniv, E., Dagan, Y. Link between the Superconducting Dome and Spin-Orbit Interaction in the (111) $\text{LaAlO}_3/\text{SrTiO}_3$ interface. arXiv:1706.01717.
- [26] Davis, S., Huang, Z., Han, K., Ariando, Venkatesan, T., Chandrasekhar, V. Superconductivity and Frozen Electronic States at the (111) $\text{LaAlO}_3/\text{SrTiO}_3$ Interface. *Phys. Rev. Lett.* **119**, 237002 (2017).
- [27] Biscaras, J., Hurand, S., Feuillet-Palma, C., Rastogi, A., Budhani, R. C., Reyren, N., Lesne, E., Lesueur, J. and Bergeal, N. Limit of the electrostatic doping in two-dimensional electron gases of LaXO_3 ($X = \text{Al, Ti}$)/ SrTiO_3 . *Sci. Rep.* **4**, 6788 (2014).

- [28] Hurand, S., et al. Field-effect control of superconductivity and Rashba spin-orbit coupling in top-gated $\text{LaAlO}_3/\text{SrTiO}_3$ devices. *Sci. Rep.* **5**, 12751 (2015).
- [29] Singh, G., Jouan, A., Hurand, S., Feuillet-Palma, C., Kumar, P., Dogra, A., Budhani, R., Lesueur, J., and Bergeal, N. Effect of disorder on superconductivity and Rashba spin-orbit coupling in $\text{LaAlO}_3/\text{SrTiO}_3$ interfaces. *Phys. Rev. B* **96**, 024509 (2017).
- [30] Mattis, C. and Bardeen, J. Theory of the Anomalous Skin Effect in Normal and Superconducting Metals. *Phys. Rev.* **111**, 412 (1958).
- [31] Dressel, M., Electrodynamics of Metallic Superconductors. *Adv. Condens. Matter Phys.*, **2013**, 104379 (2013).
- [32] Kogan, V. G., Martin, C., Prozorov, R. Superfluid density and specific heat within a self-consistent scheme for a two-band superconductor. *Phys. Rev. B* **80**, 014507 (2009).
- [33] Kim, H., Tanatar, M. A., Yoo Jang Song, Yong Seung Kwon, Y. S. and Prozorov, R. Nodeless two-gap superconducting state in single crystals of the stoichiometric iron pnictide LiFeAs . *Phys. Rev. B* **83**, 100502(R) (2011).
- [34] Binning, G., Baratoff, A., Hoenig, H. E., Bednorz, J. C., Two-Band Superconductivity in Nb-Doped SrTiO_3 . *Phys. Rev. Lett.* **45**, 1352 (1980).
- [35] Fernandes, R. M., Haraldsen, J. T., Wölfle, P. and Balatsky, A. V. Two-band superconductivity in doped SrTiO_3 films and interfaces. *Phys. Rev. B* **87**, 014510 (2013).
- [36] Trevisan, T. V., Schütt, M., Fernandes, R. M. Unconventional multi-band superconductivity in bulk SrTiO_3 and $\text{LaAlO}_3/\text{SrTiO}_3$ interfaces. arXiv:1803.02389v1 (2018)
- [37] X. Lin *et al.*, Critical Doping for the Onset of a Two-Band Superconducting Ground State in $\text{SrTiO}_{3-\delta}$, *Phys. Rev. Lett.* **112**, 207002 (2014).
- [38] Swartz A. G., Inoue, H., Merz, T. A., Hikita Y., Raghu, S., Devereaux, T. P., Johnstone, S. and Hwang, H. Y. Polaronic behavior in a weak-coupling superconductor. *PNAS*, **115**, 1475-1480 (2018).
- [39] M. Thiemann *et al.*, Single-gap superconductivity and dome of superfluid density in Nb-doped SrTiO_3 , arXiv:1703.04716, to appear on *Phys. Rev. Lett.* (2018).
- [40] Pesquera, D. *et al* Two-Dimensional Electron Gases at $\text{LaAlO}_3/\text{SrTiO}_3$ Interfaces: Orbital Symmetry and Hierarchy Engineered by Crystal Orientation. *Phys. Rev. Lett.* **113**, 156802 (2014).
- [41] Mazin, I. I., Singh, D. J., Johannes, M. D., Du, M. H. Unconventional Superconductivity with a Sign Reversal in the Order Parameter of $\text{LaFeAsO}_{1-x}\text{F}_x$. *Phys. Rev. Lett.* **101**, 057003 (2008).
- [42] Hirschfeld, P. J. , Korshunov, M. M. , Mazin, I. I. Gap symmetry and structure of Fe-based superconductors. *Rep. Prog. Phys* **74**, 124508 (2011).
- [43] Wang, F. , Lee, D.-H. The electron-pairing mechanism of iron-based superconductors. *Science* **332**, 200-204 (2011).
- [44] Prozorov, R. and Kogan, V. G. London penetration depth in iron-based superconductors. *Rep. Prog. Phys* **74**, 124505 (2011).
- [45] Hanaguri, T., Niitaka, S., Kuroki, K., Takagi H. Unconventional s-Wave Superconductivity in $\text{Fe}(\text{Se}, \text{Te})$. *Science*, **328**, 474-476 (2010).
- [46] Sprau, P. O. *et al.* Discovery of orbital-selective Cooper pairing in FeSe . *Science*, **357**, 75-80 (2017).
- [47] Kogan, V. G. and Prozorov, R. Interband coupling and nonmagnetic interband scattering in $\pm s$ superconductors. *Phys. Rev. B* **93**, 224515 (2016).
- [48] Chen, C.-T., Tsuei, C. C., Ketchen, M. B., Ren, Z.-A., Zhao, Z. X. Integer and half-integer flux-quantum transitions in a niobium-iron pnictide loop. *Nat. Phys.* **6**, 260 (2010).
- [49] Bell, C., Harashima, S., Kozuka, Y., Kim, M., Kim, B. G., Hikita, Y., Hwang, H. Y., Dominant Mobility Modulation by the Electric Field Effect at the $\text{LaAlO}_3/\text{SrTiO}_3$ Interface. *Phys. Rev. Lett.* **103**, 226802 (2009).
- [50] Wang, Z. *et al.* Anisotropic two-dimensional electron gas at SrTiO_3 (110). *Proc. Natl. Acad. Sci.* **111**, 3933-7 (2014).

Methods

Sample preparation

The 10 u.c. thick LaAlO_3 film was grown by pulsed laser deposition ($\lambda = 248$ nm) monitored by reflection high-energy electron diffraction (RHEED). The substrate was heated from room temperature to deposition temperature (850°C) in an oxygen partial pressure $P(\text{O}_2) = 0.1$ mbar. During deposition, the LaAlO_3 was grown under a pressure $P(\text{O}_2) = 10^{-4}$ mbar and a 1 Hz repetition rate, with laser pulse energy of around 26 mJ. At the end of the deposition, the sample was cooled down in oxygen rich atmosphere to minimize the formation of oxygen vacancies that could lead to extrinsic mechanisms of conduction. More specifically, the samples were cooled from $T = 850^\circ\text{C}$ to 750°C under a pressure $P(\text{O}_2) = 0.3$ mbar and under $P(\text{O}_2) = 200$ mbar from $T = 750^\circ\text{C}$ down to room temperature, including a dwell time of 1 hour at 600°C .

Hall effect and gate capacitance.

The (110)-oriented $\text{LaAlO}_3/\text{SrTiO}_3$ interface displays a Hall effect linear with magnetic field for $V_G < V_G^{\text{opt}} = -10\text{V}$ as expected for single band transport. For $V_G > V_G^{\text{opt}}$, a nonlinear Hall effect is observed due to the filling of a second band (Supplementary Figure 1) [12, 29]. The carrier density $n_{\text{Hall}} = \frac{B}{eR_{\text{Hall}}}$, reported in Fig.1e of the main text, which is extracted from R_{Hall} in the limit $B \rightarrow 0$, is only meaningful in the linear regime. However, the correct variation of carrier density as a function of V_G can be retrieved from the charging curve of the capacitor given by the integral of the gate capacitance $C(V_G)$:

$$n_{2\text{D}}(V_G) = n_{\text{Hall}}(V_G = -120\text{V}) + \frac{1}{eA} \int_{-120}^{V_G} C(V_G) dV \quad (4)$$

where A is the area of the sample. As shown in Figure 1 of the main text, $n_{2\text{D}}$ matches n_{Hall} in the single-band regime ($V_G < V_G^{\text{opt}}$) and extrapolates the curve in the two-band regime.

Reflection coefficient measurement and calibration

A directional coupler is used to guide the microwave signal from the input port to the sample through a bias-tee, and to separate the reflected signal which is amplified by a low-noise cryogenic HEMT amplifier before reaching the output port [22]. The complex transmission coefficient $S_{21}(\omega)$ between the two ports is measured with a vector network analyzer. Standard microwave network analysis relates the reflection coefficient of the RLC sample circuit $\Gamma(\omega)$ to the measured $S_{21}(\omega)$, through complex error coefficients that can be determined by a calibration. In this experiment, the microwave set-up was calibrated by using as references, the impedances Z_c of the sample circuit in the normal state of the 2-DEG for different gate values. The complex

reflection coefficient $\Gamma(\omega)$ is given by

$$\Gamma(\omega) = \frac{A^{\text{out}}(\omega)}{A^{\text{in}}(\omega)} = \frac{Z_c(\omega) - Z_0}{Z_c(\omega) + Z_0} \quad (5)$$

where A^{in} and A^{out} are the complex amplitudes of incident and reflected waves and $Z_0 = 50 \, \Omega$ is the characteristic impedance of the CPW transmission line. A reflection measurement gives therefore a direct access to the circuit impedance $Z_c(\omega)$. Supplementary Figure 2 shows the magnitude of the reflection coefficient Γ as a function of frequency and gate voltage at $T=450$ mK. The resonance manifests itself as a dip in the magnitude of $\Gamma(\omega)$ accompanied by a 2π phase shift. The value of C_{sto} which is gate dependent because of the electric field dependence of the dielectric constant of the SrTiO_3 substrate can be determined from the resonance frequency $\omega_0 = \frac{1}{\sqrt{L_1 C_{sto}}}$ for each value of the gate voltage.

Supplementary Material

Supplementary Note 1 : Two-band superfluid stiffness analysis

The temperature dependence of the normalised superfluid stiffness in the OD regime was analysed using the model developed in reference [32]. We consider two superconducting bands with density of states $N_{1,2}$ and interband coupling constants $\lambda_{11(22)}$. In addition, we add a small interband coupling between the two bands characterised by the constants $\lambda_{12(21)}$. In this BCS approach, the superconducting T_c is determined by the following equation :

$$1.76k_B T_c = 2E_D \exp\left(-\frac{1}{\tilde{\lambda}}\right) \quad (6)$$

where $E_D=400\text{K}$ is the Debye energy [?] and $\tilde{\lambda}$ the effective coupling constant given by

$$\tilde{\lambda} = \frac{2(\lambda_{11}\lambda_{22} - \lambda_{12}\lambda_{21})}{\lambda_{11} + \lambda_{22} - \sqrt{(\lambda_{11} - \lambda_{22})^2 + 4\lambda_{12}\lambda_{21}}} \quad (7)$$

For the interband coupling terms we assume that $\frac{\lambda_{12}}{n_2} = \frac{\lambda_{21}}{n_1}$, where $n_1 = \frac{N_1}{N_1+N_2} \simeq 0.6$ and $n_2 = \frac{N_2}{N_1+N_2} \simeq 0.4$ are the density of states weight in each band, which are determined from the average in-plane masses (see Supplementary Note 2). We introduce the dimensionless gap energies

$$\delta_\nu = \frac{\Delta_\nu}{2\pi T} \quad (8)$$

which is given by solving self-consistently the two following equations

$$\delta_\nu = \sum_{\mu=1,2} \lambda_{\nu\mu} \delta_\mu \left(\frac{1}{\tilde{\lambda}} + \ln \frac{T_c}{T} - A_\mu \right) \quad (9)$$

$$A_\mu = \sum_{n=0}^{\infty} \left(\frac{1}{n+1/2} - \frac{1}{\sqrt{\delta_\mu^2 + (n+1/2)^2}} \right) \quad (10)$$

For each band the temperature dependence of the associated normalized stiffness is derived from the dimensionless gap energy δ_ν

$$j_{s\nu} = \delta_\nu^2 \sum_{n=0}^{\infty} [\delta_\nu^2 + (n+1/2)^2]^{-3/2} \quad (11)$$

The total normalized stiffness is the sum of the contributions of each band

$$j_s = \gamma j_{s1} + (1 - \gamma) j_{s2} \quad (12)$$

where the γ coefficient accounts for the weight of each band in the superfluid condensate. Data shown in Figure 4 of the main text has been fitted using the relations (6) and (7). Note that in this pure BCS approach, the effect of fluctuations has not been included. Supplementary Figure

5 shows the evolution of the γ coefficient with the gate voltage.

In Supplementary Figure 6 we show the doping dependence of the dimensionless coupling constant extracted from the analysis of the superfluid stiffness. As explained in the method section, $\tilde{\lambda}$ is the effective coupling determining the T_c . In the single-band case, it coincides with λ_{11} , while for the multiband regime it is given by Eq. (2). As mentioned in the main text, the analysis of the temperature dependence of the superfluid density relies mainly on the relative band filling and on the gap values, so it is a robust finding rather insensitive to the presence of disorder. On the other hand, $\Delta_\nu(T)$ must be derived using a specific model for the superconducting state. To simplify the analysis, we relied on the Eq.s (3)-(5), where the gap are computed for a multiband model in the absence of disorder. In this case, the only way to obtain a decrease of the gap values at $T = 0$ is to reduce the coupling constants for increasing density, as shown in In Supplementary Figure 6. However, a similar result could be possibly obtained by using constant superconducting couplings and introducing the effect of disorder. Indeed, as recently discussed in Ref. [36], in the presence of disorder a s_\pm superconducting state is strongly affected by the onset of occupancy of the secondary band. Indeed, interband impurity scattering is pair breaking in a s_\pm superconductor, leading to a gradual suppression of both the critical temperature and of the superconducting gap across the Lifshitz transition. A quantitative analysis of this effect requires however a detailed analysis of a dirty multiband model that is well beyond the scope of the present work.

Supplementary Note 2 : Interfacial band structure simulation

The filling and the confinement of each t_{2g} band are determined by solving self-consistently the schrödinger and the Poisson equations as described in the supplementary material of reference [12]. The hopping terms in Fig 1a. were taken to be $t_1 = -320\text{meV}$ and $t_2 = -16\text{meV}$, which correspond to the masses $m_{001}^{xz,yz} = -\frac{\hbar^2}{2a^2 t_1} \simeq 0.7m_0$ for the $d_{xz/yz}$ orbitals and $m_{001}^{xy} = -\frac{\hbar^2}{2a^2 t_2} \simeq 14m_0$ for the d_{xy} orbitals along the (001) direction of the conventional (001)-oriented interfaces. In the (110)-oriented interfaces, the masses along the confinement direction (i. e. the (110) direction) are $m_{110}^{xz,yz} = -\frac{\hbar^2}{2a^2(t_1+t_2)} \simeq 0.65m_0$ and $m_{110}^{xy} = -\frac{\hbar^2}{4a^2 t_1} \simeq 0.35m_0$ [50]. The density of states can be determined from the in-plane masses in the (1-10) and (001) directions. For the d_{xy} orbital, $m_{001}^{xy} = -\frac{\hbar^2}{2a^2 t_2} \simeq 14m_0$ and $m_{1-10}^{xy} = -\frac{\hbar^2}{2a^2 t_1} \simeq 0.7m_0$, corresponding to an average in-plane mass $m_{\parallel}^{xy} = \sqrt{m_{001}^{xy} m_{1-10}^{xy}} \simeq 3.1m_0$ [50]. For the $d_{xz,yz}$ orbitals, $m_{001}^{xz,yz} = -\frac{\hbar^2}{2a^2 t_1} \simeq 0.7m_0$ and $m_{1-10}^{xz,yz} = -\frac{\hbar^2}{2a^2(\frac{2t_1 t_2}{t_1+t_2})} \simeq 7.3m_0$, corresponding to an average in-plane mass $m_{\parallel}^{xz,yz} = \sqrt{m_{001}^{xz,yz} m_{1-10}^{xz,yz}}$

$\simeq 2.3m_0$ [50].

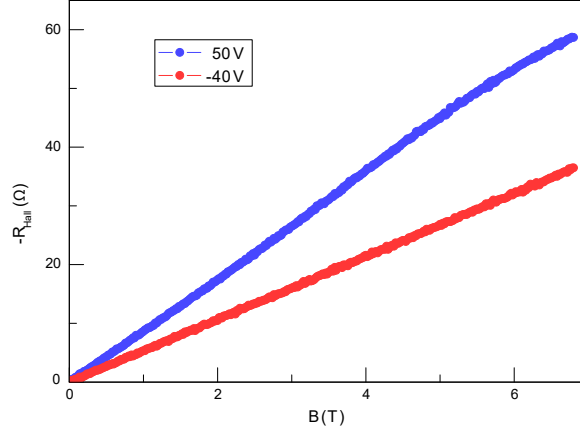


Figure 6: Hall resistance as a function of magnetic field applied perpendicular to the interface for $V_G = -40\text{V}$ (single-band) and for $V_G = 50\text{V}$ (two-band).

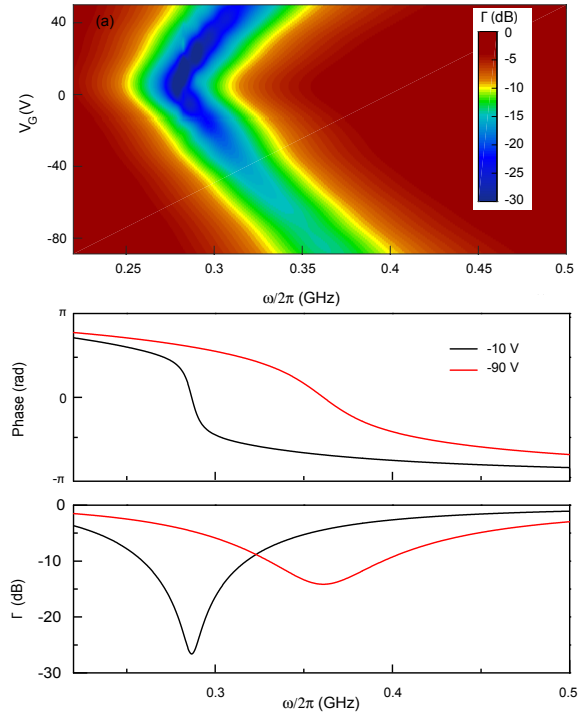


Figure 7: (a) Magnitude of Γ in dB (color scale) as a function of ω and V_G . C_{sto} takes a maximum value of 36 pF for $V_G = 0$ V. Phase (b) and magnitude (c) of Γ for $V_G = -90\text{V}$ and $V_G = -10\text{V}$.

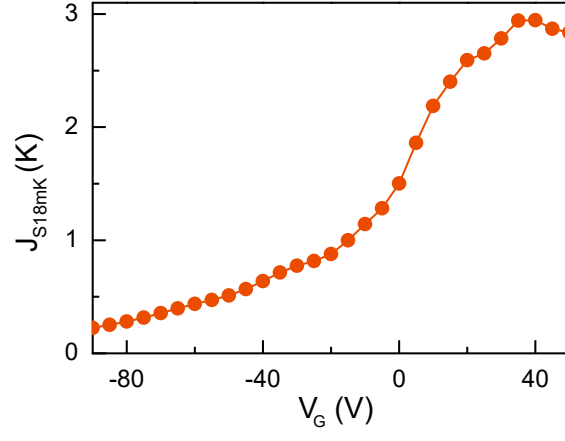


Figure 8: Gate dependence of J_s extracted from $\Gamma(\omega)$ at the lowest temperature $T \simeq 18 \text{ mK}$.

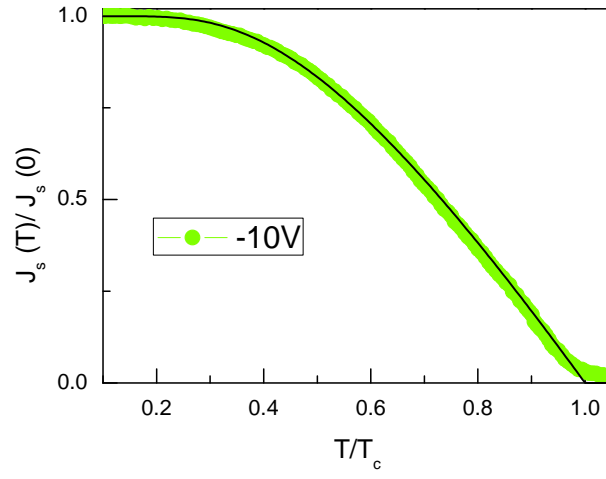


Figure 9: Temperature dependence of normalised superfluid stiffness $j_s(T)$ at the optimal doping point $V_G = -10 \text{ V}$ fitted by a single band BCS model.

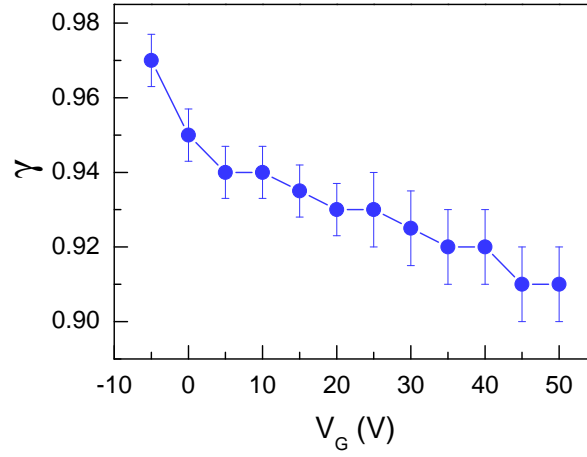


Figure 10: Gate dependence of the γ coefficient controlling the weight of each band in the superfluid stiffness (Eq. (3) in the main text).

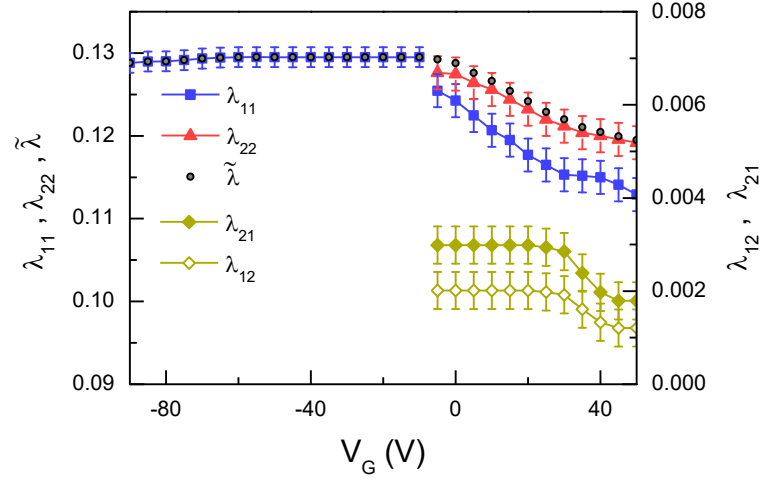


Figure 11: Gate dependence of the coupling constants in the phase diagram. The main source of pairing is the positive intraband coupling $\lambda_{11(22)}$ with a small interband coupling $\lambda_{12(21)}$ which can be either positive (attractive) or negative (repulsive). The values of the coupling constants are found to be comparable to the rare values reported in the literature for bulk SrTiO_3 [35]